remote sensing

MDPI

Article

The Spatial Analysis of Vegetation Cover and Permafrost Degradation for a Subarctic Palsa Mire Based on UAS Photogrammetry and GPR Data in the Kola Peninsula

Natalya Krutskikh [1], Pavel Ryazantsev [2,*], Pavel Ignashov [3] and Alexey Kabonen [4]

[1] Institute of Geology, Karelian Research Centre of RAS, 185910 Petrozavodsk, Russia
[2] Department of Multidisciplinary Scientific Research, Karelian Research Centre of RAS, 185910 Petrozavodsk, Russia
[3] Institute of Biology, Karelian Research Centre of RAS, 185910 Petrozavodsk, Russia
[4] Institute of Forestry, Mining and Construction Sciences, Petrozavodsk State University, 185910 Petrozavodsk, Russia
* Correspondence: chthonian@yandex.ru

Abstract: Subarctic palsa mires undergo substantial transformation under climate impacts, and today a reliable marker of their degradation is the vegetation cover. We studied the correspondence between the surface traits of palsa degradation, as expressed in the vegetation composition, and the interior condition of permafrost within subarctic palsa mires in the central part of the Kola Peninsula. We have employed a set of methods to collect the data, including geobotanical relevés, unmanned aerial system (UAS) photogrammetry, and ground-penetrating radar (GPR) survey. Based on RGB orthophoto values and morphometric variables, we produced a land cover classification (LCC) consistent with the vegetation classes identified during field measurements. The outcome proves that the additional morphometric predictors improve the accuracy of classification algorithms. We identified three major patterns in GPR cross-sections defining (i) permafrost in palsas, (ii) water saturated peat, and (iii) the regular peat layer. As a result, our GPR data demonstrated a high correlation with land cover classes and pointed to some vegetation features controlled by the peat deposit inner structure. Under our results, palsas with thawing permafrost can be appraised using sequences of LCC. This is primarily the lichen hummock—tall shrub—carpet vegetation (LH–TSh–C) sequence from palsa top to foot. We have also detected an asymmetric configuration of permafrost in some palsas in the west-to-east direction and hypothesized that it can relate to the wind regime of the area and snow accumulation on the eastern slopes. Our results highlight that the combined application of the remote UAS photogrammetry and GPR survey enables a more precise delineation of the lateral degradation of palsas.

Keywords: digital elevation model; GPR cross-sections; patterns; machine learning; land cover classification; morphometric predictors; Lovozero

Citation: Krutskikh, N.; Ryazantsev, P.; Ignashov, P.; Kabonen, A. The Spatial Analysis of Vegetation Cover and Permafrost Degradation for a Subarctic Palsa Mire Based on UAS Photogrammetry and GPR Data in the Kola Peninsula. *Remote Sens.* **2023**, *15*, 1896. https://doi.org/10.3390/rs15071896

Academic Editor: Radosław Juszczak

Received: 15 February 2023
Revised: 24 March 2023
Accepted: 30 March 2023
Published: 31 March 2023

1. Introduction

Fennoscandian subarctic palsa mires are vulnerable ecosystems undergoing significant transformation under climate impacts [1–7]. Modern bioclimatic models predict that the territory of Fennoscandia may, in the mid-run (20–40 years), become climatically unsuitable for peatland permafrost [8,9]. Recent studies likewise highlight the complex dynamics of the permafrost of high-latitude peatlands and point to the need for a comprehensive approach in particular to their ecohydrological study [10,11]. Degradation of discontinuous permafrost in Fennoscandia is primarily attributed to a growing snow cover thickness, while air temperature has remained statistically unchanged [12]. This current situation requires a thorough monitoring of palsa mires to predict potential ecological damage from their degradation and to work out mitigation strategies.

Arctic- and subarctic-type palsa mires have a perennial cryogenic core at the base of the peat deposit. They are common at the southern limit of sporadic permafrost and require specific environmental conditions to remain stable [13–15]. Palsas are peat-covered, dome-shaped frost mounds forming specific landform types that are typical for low-gradient postglacial landscapes, and their cyclicity of development, stages of formation, and processes of thermal erosion make them objects of scientific interest [16,17]. Palsa mires are usually noted for high morphological diversity and their microrelief features can be formed by thermokarst and thermal erosion processes [18]. The peatland's geomorphology, hydrological conditions, and topography of the underlying substrate influence the vegetation diversity, peat accumulation, and formation of higher palsas [19]. Hence, the landscape features, morphology, hydrology, and vegetation composition must be considered when analyzing palsa mire dynamics [20,21]. An important marker for the permafrost degradation assessment in palsa mires is the vegetation composition [22]. Total loss of the frozen core in hummocks leads to more active development of the subshrub canopy, which then promotes the woody vegetation settlement [23]. Another possible vegetation succession is the mosses' replacement with herbaceous and subshrub communities. Meanwhile, mosses play a key role in long-term processes in arctic ecosystems: peat accumulation, the development of microtopography, and permafrost stability [24]. The above processes form an important indicator of a profound change in mires' ecosystem condition. Apart from the peat moisture increase one would expect from permafrost thawing, the ratio between the warmed active layer and the underlying frozen layer may promote drying up through evapotranspiration with effects on the vegetation cover [25].

Objects of particular interest in terms of palsa collapse monitoring are mires at the southern boundary of the permafrost region. The reason is the higher rates of palsa decay and the associated significant changes, so that individual trends of ecosystem change can be detected through observations of a short duration [5,6]. In north-eastern Fennoscandia, permafrost occurs in the Kola Peninsula [26,27]. The palsa mires of the Kola Peninsula have been studied in fewer numbers and in less detail than those in the neighboring regions of Norway, Sweden, and Finland [28], where they are under long-term monitoring. It was previously assumed that the palsa mires of the Kola Peninsula have been stable over the past 80 years [29]. This conclusion cannot be reliable, however, since the assessment was based only on the mean annual temperature and thickness of the active layer on palsas. It is currently known that palsa mires undergo predominantly lateral permafrost degradation [5], while in the vertical projection, including the active layer, the seasonal growth of palsa permafrost has a great influence according to a model suggested by Seppälä [15]. Meteorological observations on the Kola Peninsula over 50 years specified an average temperature rise of 2.38 $\pm$ 1.08 °C and revealed an increase in the humidity in springtime and its decline in autumn [30]. Hence, we have to expect active palsa mire degradation to happen in this Arctic region as well in the short term. A process to note is all vegetation element transformations in the palsa mires of the Kola Peninsula, which point to the stability issue of permafrost landforms under present-day climatic conditions [7,31,32].

The areal loss of palsas is non-linear, often rapid and episodic [21]. Therefore, remote sensing methods are becoming increasingly important in the assessment of permafrost degradation in palsa mires [33,34]. Landscape research based on such methods is relevant for the Kola Peninsula, especially in central and eastern parts, where transport infrastructure for ground observations is underdeveloped. A useful tool in the study and modeling of natural ecosystem transformation is the land cover classification (LCC) developed using remote sensing data [35]. Land cover maps for arctic and subarctic regions are widely used in vegetation assessments [33,36–40] and to predict permafrost thawing and carbon stores in soils [41–44]. The land cover and topographic characteristics, as well as subsurface changes, are essential components to be documented in a comprehensive study of permafrost. For instance, palsa mires have been studied by methods such as combinations of LiDAR and ERT [45,46] and ERT and GPR [47,48]. A significant role in the assessment of permafrost degradations should also be given to the control of the hydrological conditions in the peat

deposit based on geophysical monitoring, considering that the drainage effect can vary the ground temperature in palsa mires by up to 2 °C [49].

Conformant to this concept, we combined aerial photogrammetry with in situ vegetation relevé surveying and GPR surveying with manual probing. Our purpose was to evaluate the correspondence between the surface traits of palsas' degradation expressed in the landscape features and vegetation composition and the permafrost interior condition and peat hydrology based on remote sensing methods.

2. Study Site

The Lovozero palsa mire we surveyed lies in the sporadic permafrost region of the Kola Peninsula [27], near the town of Lovozero, Murmansk Region (WGS 84 68.011869°N; 35.084062°E), at 160 m elevation (Figure 1). It is a component part of a large mire system where flat-topped frozen peat hummocks and wet melted flarks alternate. The palsas are ridge-shaped in plan view, 0.7–1.2 m (up to 2.0 m) high, occupying 60–70% of the site area, while active layer thickness on hummocks ranges within 20–60 cm. The peat deposit in the mire is estimated to be 0.8–2.6 m thick, and sand and sandy loam underlies it. There is no doubt that palsas in this mire are degrading, but we see no large areas with crack formation and peat surface erosion. The vegetation on hummocks and in flarks differs both with regard to the key taxa composition and in the nutrition and moisture status. Oligotrophic subshrub–moss–lichen communities dominate on hummocks, and mesotrophic sedge–cottongrass–sphagnum communities on flarks [50]. A previous hydrological monitoring survey of the Lovozero mire showed there was no water table in the palsas throughout most of the season since the water from snowmelt and rainfall rolled down the permafrost layer boundary into flarks [51].

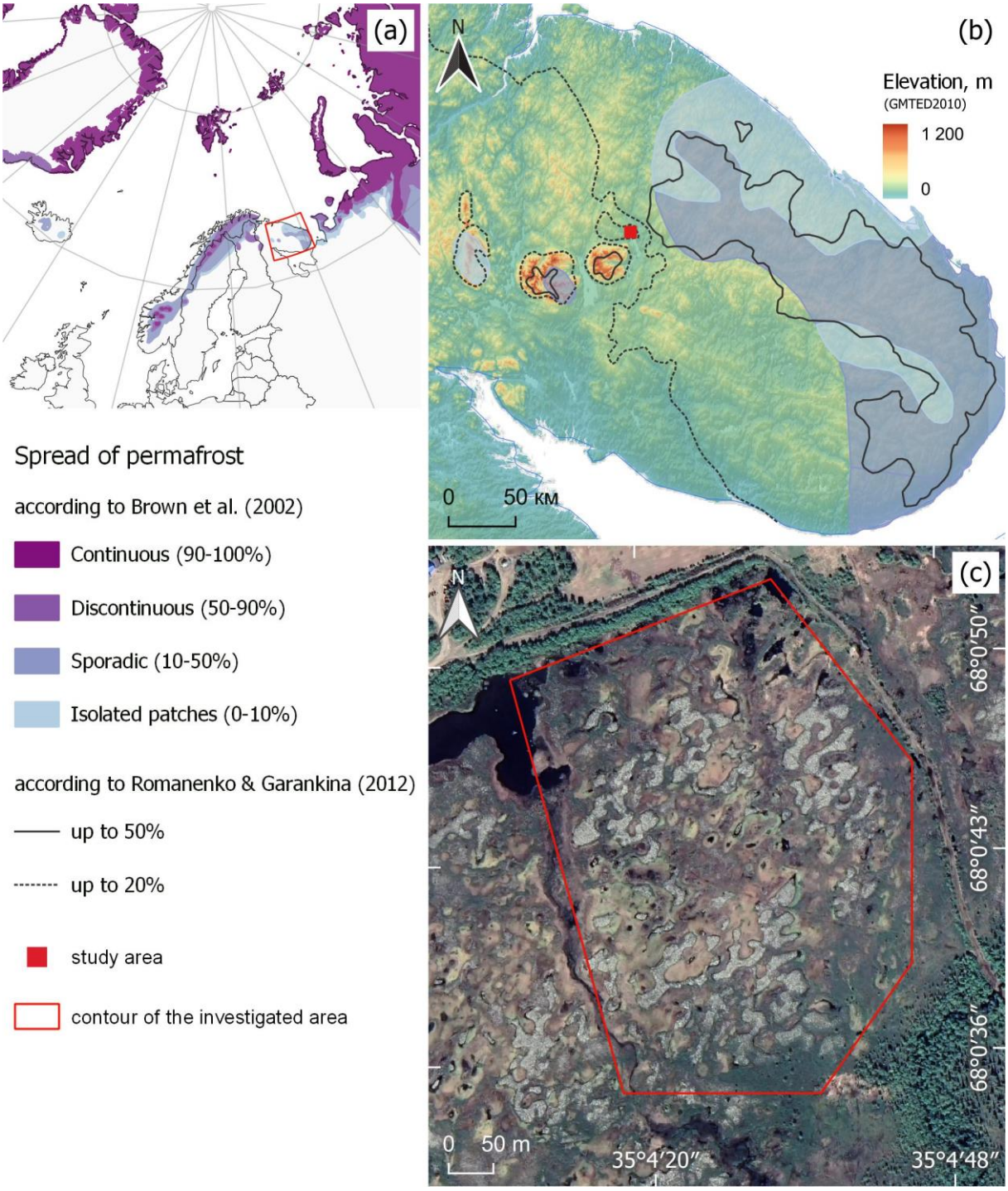

Figure 1. Location of the surveyed palsa mire on the Kola Peninsula, an overview of the distribution of permafrost abundance (**a**), the regional elevation map according to GMTED2010 [52] (**b**), and the site outline on the Google satellite image (**c**). Brown et al. (2002) [26], Romanenko & Garankina (2012) [27].

3. Methods

We carried out all the fieldwork in July 2021, during the most active vegetation growing season. The surface area of the site surveyed in the Lovozero mire was 0.3 km^2. At the initial stage of the research, we conducted aerial photography. Next, we performed ground observations. In addition to taking ground-penetrating radar (GPR) measurements and

relevés, ground activities included the documentation of permafrost thawing traits and peat erosion areas (Figure 2).

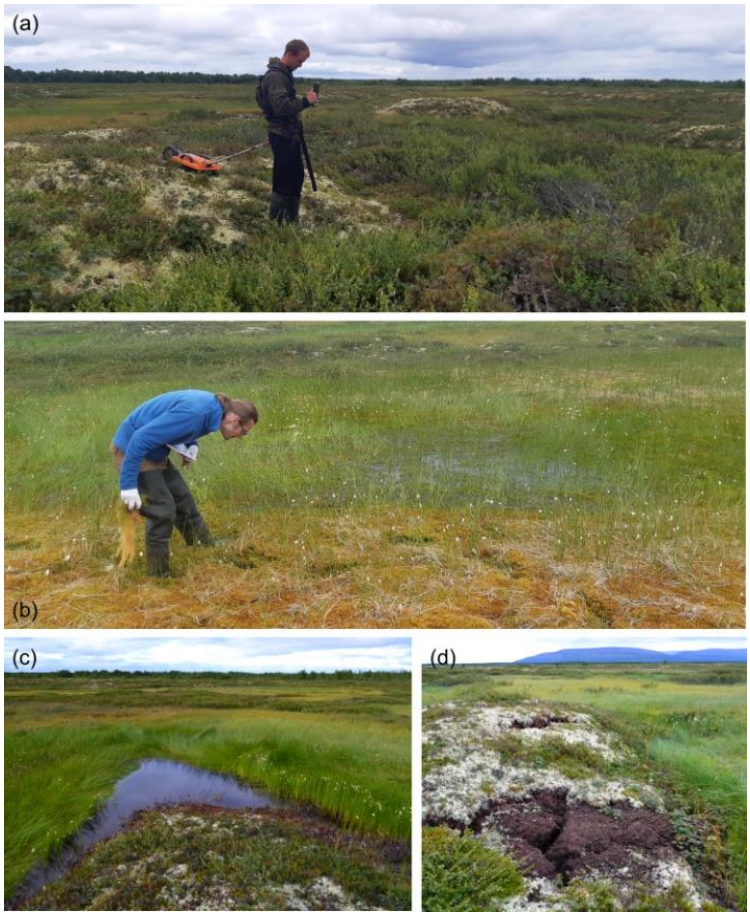

Figure 2. Photographs from fieldwork on Lovozero mire: GPR surveying of palsas (**a**), relevé sampling in a flark (**b**), meltwater accumulation area with the associated vegetation succession (**c**), peat erosion area on hummock slope (**d**).

4. UAS Photogrammetry

Unmanned aerial systems (UASs) have been successfully used in vegetation monitoring [38,53–56]. Their key benefits are the relatively inexpensive maintenance and high-resolution images as the output. Using UAS-derived orthophotos and digital elevation models (DEMs), researchers can delineate palsa hummocks at 0.03–0.05 m grid cell resolution and explore their attributes [34,57]. The usage of UASs has proved to work well in subarctic palsa mire surveys, delivering high-resolution imagery [33]. High-resolution DEMs were produced using structure-from-motion (SfM) photogrammetry, which has a proven performance for natural objects of complex topography [58].

We took aerial photos using DJI Phantom 4 Pro V2.0. This UAS is fitted with an inertial measurement unit (IMU) and GPS, which determine its position and height during flight so that the geographic coordinates of the center of the photos are known (the claimed accuracy of GPS positioning is 0.1 to 1.5 m). The drone is also equipped with an enhanced FC6310S digital camera with a wide-angle lens and 1″ 20 MP CMOS sensor. The system produces 5472 × 3648-pixel RGB images, and the spatial resolution of the resultant composite image depends on the drone flight altitude and photo overlap.

As the mire is rather large and the battery capacity (25 min at maximum) limits the UAS flight time, the territory to be covered by the aerial survey was divided into two adjacent 350 × 300 m plots using the Pix4DCapture flight planning application (Figure S1). The Double Grid flight mode was applied (frontal and lateral overlaps of 80–70%, flight

altitude of 70 m, camera tilt angle of 80°). The flights produced 1014 images with a 1.96 cm/px resolution. We realized photogrammetry processing with Agisoft Metashape Professional software and pooled aerial photos from two flights into one project. The processing algorithm included several stages: image alignment, building dense cloud, raster DEM, and orthophoto with WGS84 referencing. High-quality processing settings were selected at all stages.

The drone flights occurred without the use of a GNSS receiver and ground control points. This, as expected, led to low rates of accuracy in fixing photographic centers in the WGS-84 system. The average errors in the coordinates of the centers were 0.57 m for longitude and 0.88 m for latitude, which correspond to the declared technical characteristics of the selected UAS (1.5 m). Our study did not require obtaining a high-precision reference to the global positioning system. However, we needed an accuracy sufficient for DEM reconstruction during photogrammetric processing and for further use in data processing. Thus, to achieve the goal, we used the local coordinate system without high-precision binding to global positioning. During photogrammetric processing, the average discrepancy (re-projection error—the distance between the initial projection of a point on the image and the projection of the reconstructed three-dimensional point on the same image) for two flights was 0.53 px with a size of 2.41 × 2.41 µm. GPS inaccuracy and small errors in photogrammetric processing had a low effect on the quality of the final DEM.

The photogrammetry processing results specified in Table 1 formed the input for machine learning for the aim of land cover classification (LCC). To enable local-scale land cover classification, the orthophoto and DEM spatial resolution was reduced to 0.5 m/px. We have changed the resolution of the images to reduce the size and improve the speed of data processing. Moreover, reducing the resolution allows you to filter images and exclude noise during further classification. We conducted the calculation of the pixel values of the transformed image using the "nearest neighbor" method.

Table 1. Results of photogrammetry processing of UAS data.

	Orthophoto	**DEM**
Spatial resolution, cm/px	1.96	3.92
Number of channels	3 (RGB)	1

5. Ground-Penetrating Radar Measurements

Ground-penetrating radar (GPR) surveying is a non-invasive geophysical method in which nanosecond fixed-frequency electromagnetic (EM) pulses are emitted into the subsurface and the returning signal reflected by interior interfaces and local heterogeneities in the ground is recorded and analyzed [59]. The characteristics that define EM wave propagation are the dielectric constant and electric conductivity. The GPR method works well in permafrost studies through the contrastive electrophysical properties of the frozen ground in regions with discontinuous permafrost [60–62], palsa hummocks included [63,64]. As shown by seasonal GPR measurements in palsa mires, summer GPR cross-sections reveal only the upper boundary of permafrost in palsas, whereas the bottom boundary is detectable in wintertime records [65]. Studies of Yildiz et al. [66] on a combined application of UAS photogrammetry and GPR for quantifying snow cover thickness have illustrated that this approach can be promising for palsa research.

We performed field surveys using GPR OKO-2 with an antenna unit with a 400 MHz central frequency (Logis-Geotech, Moscow, Russia). With this frequency, the subsurface can be probed down to 5 m depth at a vertical resolution of ±5 cm. The time window was 200 ns; the step size for probing the profile was 10 cm. We performed the final GPR data processing in GeoScan32. Before the interpretation, we applied the main record processing tools: zero time correction; bandpass filter and mean subtraction—to eliminate DC shift and signal saturation; amplitude gain—to compensate signal attenuation; and the selection of reflectors and velocity analysis—to delineate the actual position of interfaces in the peat

deposit. The analysis of the velocities derived from diffracted wave hyperbolic fitting found variability from 3.9 cm ns^{-1} in the high moisture part of the peat deposit to 8.6 cm ns^{-1} in its elevated, driest part. The time-section was translated to the depth-section using an average velocity value of 4.7 cm ns^{-1}. We derived the topographic correction for GPR cross-sections from the DEM obtained by the processing of UAS data. Five GPR profiles were taken in total, three of which traversed the site from west to east and the other two from north to south. With the help of manual soundings to verify the GPR data, we controlled the positions of the permafrost top in palsa hummocks and the thickness of the peat in the flarks.

6. Machine Learning for Land Cover Classification

Machine-learning methods are used in dealing with non-linear relationships between environmental parameters and remote sensing variables [43]. Machine learning encompasses an array of intellectual data analysis techniques, which can recognize patterns in datasets and predict quantitative variables. We have developed multiple algorithms for classification and forecasting. Some of the popular ones are the naive Bayes (NB) classifier, artificial neural networks (ANNs), random forests (RFs), and support vector machines (SVMs) [67,68]. These algorithms represent different supervision strategies: the NB classifier is a statistical learning algorithm, RF training is based on logic, and SVMs and ANNs are perceptron-based [69]. Reportedly, SVMs and RFs commonly outperform ANNs [70]. For LCC, we tested different strategies and therefore used three algorithms from different strategies—an NB classifier, a RF, and an SVM. The testing of the algorithms and selection of the optimal ones can improve the output of palsa mires' spatial variability and dynamics estimation.

The NB classifier is a simple classification model [71]. Using the training dataset, the algorithm estimates the mean vectors and covariance matrices for each class and then makes predictions based thereon. The SVM algorithm maps feature vectors in multidimensional space using the kernel function and plots an optimal linear discriminant function in that space [72]. The RF is a machine-learning algorithm suggested by Breiman, which is based on an ensemble of decision trees. Thus, the key underlying idea is to use a large ensemble of decision trees, each of which alone may produce classifications of rather poor quality, but, there being sufficient trees, the eventual output is quite accurate [73].

We used a spatially referenced array of environmental data as a predictor to determine the spatial properties of the study site. The predictors were RGB channel values for the orthophoto discretized to a 0.5 m resolution. We computed a DEM at a 0.5 m spatial resolution to generate additional morphometric datasets to be used as predictors in machine learning: the slope, topographic position index (TPI) [74], and topographic wetness index (TWI) [75]. The TWI is the slope and area function, which is commonly used for the quantification and topographic control of hydrological processes. Sites that have a tendency to accumulate water (large areas in catchments) and have minor slope angles will have high TWI values, whereas well-drained dry areas (steep slopes) are associated with low TWI values.

The slope is an important landscape parameter. The surface slope determines runoff and drainage, the rate of the translocation of material, erosion processes, and soil thickness. The topographic position index (TPI) compares the elevation of each cell to the mean elevation of a specified neighborhood around that cell [76]. TPI values can be standardized to produce a classification. Weiss [76] suggests the following classification of landforms:

- Valley: TPI ≤ -1 SD;
- Lower slope: -1 SD < TPI ≤ -0.5 SD;
- Flat area: -0.5 SD < TPI < 0.5 SD, slope $\leq 5°$;
- Middle slope: -0.5 SD < TPI < 0.5 SD, slope > $5°$;
- Upper slope: 0.5 SD < TPI $\leq$ 1 SD;
- Ridge: TPI > 1 SD.

The training sample for the Lovozero mire land cover comprised 120 polygons, 2 × 2 m each (4 × 4 pixels), and the polygons are evenly dispersed over the territory and belong to one of the six land cover classes. We visually interpreted the training sample according to the received orthophotomap based on ground data. Polygons were determined randomly and presented uniformly across all land cover classes; each had 20 training points. In addition to open water (W), we distinguished five vegetation classes: lichen hummock vegetation (LH), carpet vegetation (C), tall graminoid vegetation (TG), moist hummock vegetation (MH), and tall shrub vegetation (TSh) (Figure 3). The classification quality assessment was also based on a set of 120 ground control points. The control points were chosen independently of the training samples. They were also visually interpreted from the orthophotomap. We produced a detailed geobotanical description for each class to control the plant species' diversity in the vegetation cover (Table 2). The overall accuracy was determined for all the land covers [77]. Geospatial analysis, raster and vector processing were realized in QGIS, accuracy was calculated using the Semi-Automatic Classification Plugin, and machine learning performed by built-in tools in SAGA [78].

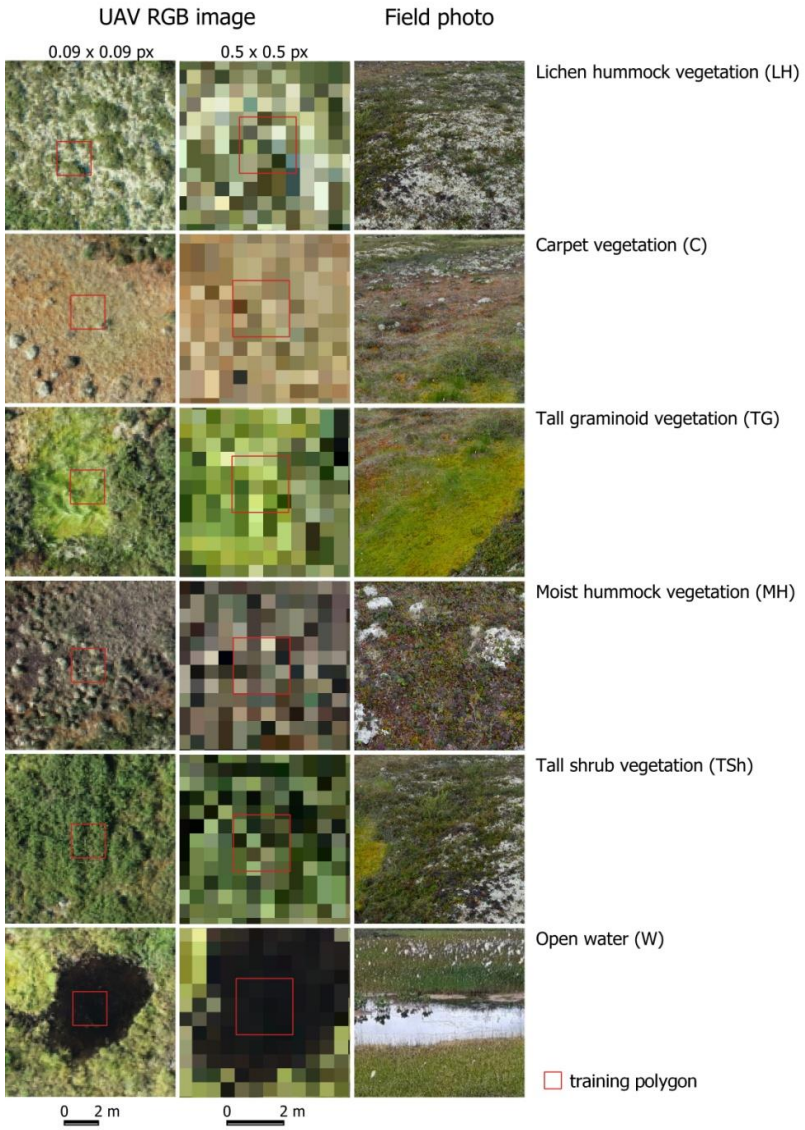

Figure 3. RGB imagery matrix for land cover classification in the surveyed site.

Table 2. Geobotanical characteristics of individual land cover classes.

Land Cover Class	Herb and Subshrub Layer	Mean Cover (%)	Moss and Lichen Layer	Mean Cover (%)
lichen hummock vegetation (LH)	*Empetrum hermaphroditum* Hagerup, *Rubus chamaemorus* L., *Vaccinium vitis-idaea* L.	20	*Cladonia* ssp., *Flavocetraria nivalis* (L.) Kärnefelt et A. Thell	90
carpet vegetation (C)	*Eriophorum vaginatum* L., *Carex limosa* L., *C. rotundata* Wahlenb.	20	*Sphagnum balticum* (Russow) C.E.O. Jensen, *Sphagnum lindbergii* Schimp.	90
tall graminoid vegetation (TG)	*Eriophorum russeolum* Fr., *Eriophorum angustifolium* Honck.	45	*Sphagnum riparium* Ångstr.	80
moist hummock vegetation (MH)	Rubus chamaemorus L., *Empetrum hermaphroditum* Hagerup, *Andromeda polifolia* L., *Eriophorum vaginatum* L.	40	*Sphagnum fuscum* (Schimp.) H. Klinggr., *Sphagnum capillifolium* (Ehrh.) Hedw.	95
tall shrub vegetation (TSh)	*Betula nana* L., *Ledum palustre* L.	70	*Pleurozium schreberi* (Willd. ex Brid.) Mitt., *Sphagnum fuscum* (Schimp.) H. Klinggr.	40

7. Results

During the first stage, we analyzed the imagery obtained by UAS photogrammetry. The final detailed orthophoto of a 0.3 km^2 area (high-resolution image, Figure S2) provided us with a set of morphological variables for the surveyed site. The DEM depicted the overall layout and shapes of the palsas and revealed a monotonic elevation trend on the study site (Figure 4a). We found the overall terrain elevation grew by 3 m from north to south, with the largest palsas concentrated in the southern part. The detected elevation trend is associated with an increase in the thickness of the peat deposit, which grew in the paleolake basin. Palsa hummocks were predominantly 1–1.5 m high, and their area varied from 190 to 1700 m^2. Such morphology is associated with the general patterns of peat deposit growth, which involves peat accumulation and the accompanying deposition of water, including in the permafrost form. The surface slope in the area ranged from 1 to 10°, with an average of 3.6°. The slopes of the palsas proved to be comparable, notwithstanding their size variation (Figure 4b). Apparently, the frost heaving process was identical in all palsas, resulting in equal uplift amplitudes. This means the initial parameters (peat temperature, moisture content, and thickness) were equivalent to most of the peat deposit area, except for the northern and eastern margins of the site. Along the northern and eastern outline of the site, there is a byroad, which could significantly affect the hydrological situation of this mire parts (Figure 1c). As a result, in these points, we observed obvious signs of mire system transformation, including complete permafrost degradation. The TPI map clearly visualized the above factors and that all palsas on the site have a similar morphometric structure (Figure 4c). The TWI distribution was quite complex and mosaic, especially in low-lying areas, where small-scale drainage channels have formed (Figure 4d). Meanwhile, the overall TWI was low. Judging by the morphostructural slope and TPI characteristics of the surveyed palsa mire site, its center used to hold a small water reservoir, which was then drained up by permafrost and the host peat.

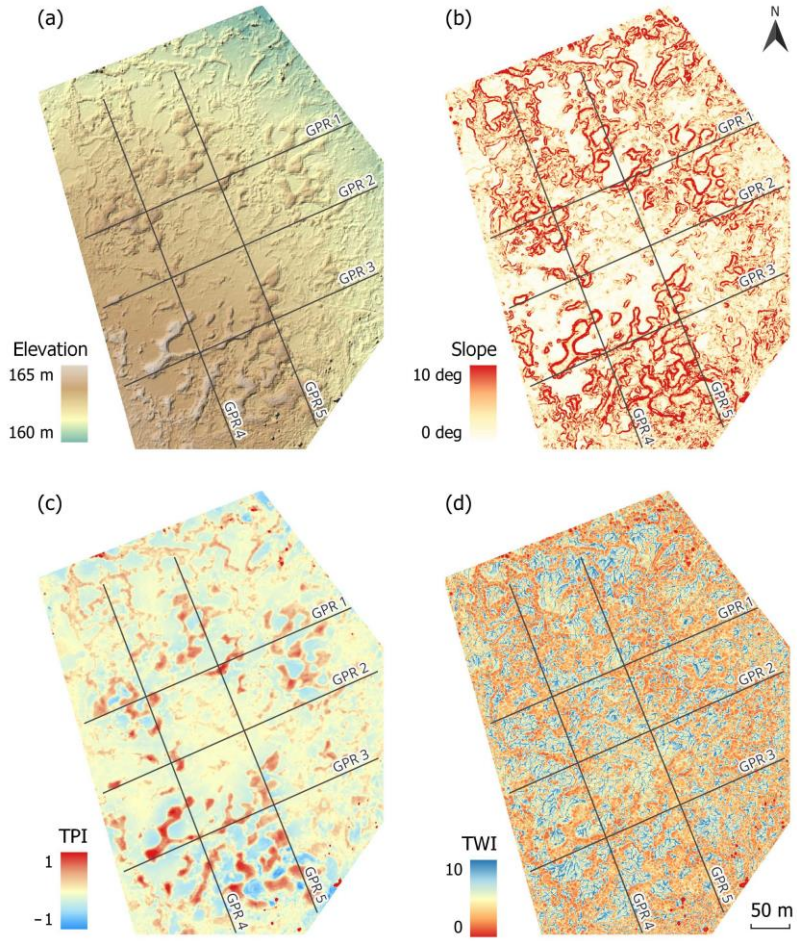

Figure 4. DEM (**a**) and morphometric dataset: slope (**b**), topographic position index (**c**), and topographic wetness index (**d**) with GPR profile lines.

Our next step was to study the statistics on the environmental parameters in each land cover class on the site according to the training sample (Figure 5). Analysis revealed that subshrub–lichen vegetation (LH) was mainly localized on palsa tops with an average elevation of 163.3 m and therefore had the highest average TPI = 0.5 and a very low TWI = 3.4. Cottongrass–sedge–sphagnum carpet vegetation (C) mostly grew in the hollows superseding collapsed palsas, which had a TPI = −0.2 and slope less than 1 deg. This class occurred chiefly at 162.6 m elevations and featured a high average TWI = 6.5. Cottongrass–sphagnum vegetation (TG) often grew at the foot of palsas with a minor slope of 2.7 deg, a medium TPI = −0.18, and, at the lowest, 162 m elevations. The identification of this class is essential as it fringes degraded palsas and is an indicator of ongoing permafrost thawing. Subshrub–sphagnum vegetation (MH) had TPI and TWI values very similar to the predictors of C and TG, while differing slightly in slope. Tall shrub vegetation (TSh) occupied palsa slopes and so had the highest average slope value (5.3 deg) and its widest range (2–8°). Other distinctions of the TSh class were the average TPI = 0.2 and the sample's lowest TWI = 3. The open water class (W) stood out the most for the lowest elevation of 161.3 m and a near-zero slope, as well as for the lowest average TPI = −0.3 and the highest TWI = 6.9. Thus, in terms of morphometric parameters, there are significant differences between the means and variances of various LCCs. We have used these differences and added morphometric parameters for automatic land cover classification.

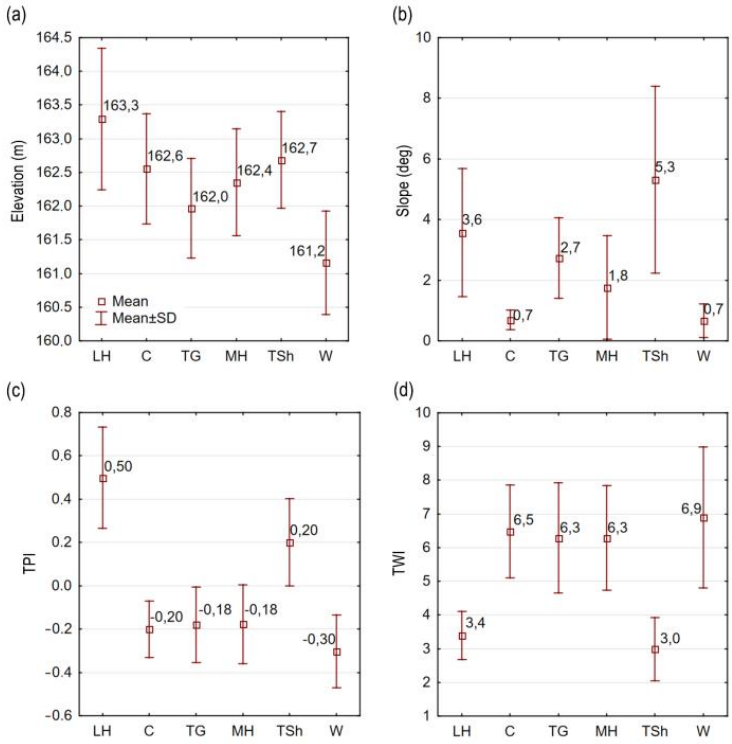

Figure 5. Means and standard deviations (SD) of morphometric variable values for training sample data (**a**)—elevation, (**b**)—slope, (**c**)—topographic position index, and (**d**)—topographic wetness index.

The LCC produced by all classification algorithms was in good agreement with the classes distinguished both by in situ relevé surveys and identified visually in the orthophotos (Figure S3). The LCC algorithms demonstrated a quite high overall accuracy, but we received the best results using the NB algorithm (Figure 6). We computed the producer accuracy to compare the algorithm's performance for each land cover class (Table S1). We found that the highest producer accuracy for most of the classes was achieved by the NB classifier (Table 3). The exceptions were the LH and C classes, which were identified the most accurately by the RF algorithm. Classification by RF delivered the worst producer accuracy levels for the classes TSh and W. The class identified the most accurately was C, probably because of the relative color evenness of the RGB pixels (Figure 3) and the near absence of slope. Shade was not a problem, as there are almost no tall plants within the site. In the plot's south, the NB algorithm classified single shadows correctly, while other algorithms did not give a good result for the southern part.

All algorithms showed that the greatest cover in the surveyed palsa site belonged to the TSh class, which was 33% of the total area on average (Table 4). This class mainly occurred along the edges, where permafrost had already thawed and the peat deposit was drier. The next most common class was MH, covering 24% of the study site, also with a localization in the zones of collapsed palsas. The classes LH, C, and TG occupied approximately equal proportions of 11–15% of the total area.

Table 3. Algorithms' classification accuracy.

Classification Algorithms	Overall Accuracy, %	Producer Accuracy					
		LH	C	TG	MH	TSh	W
NB	86.4	80.9	87.5	89.1	89.3	84.4	91.7
RF	78.7	83.4	89.4	81.3	82.8	72.1	67.6
SVM	82.5	70.7	86.5	77.9	84.8	84	89.8

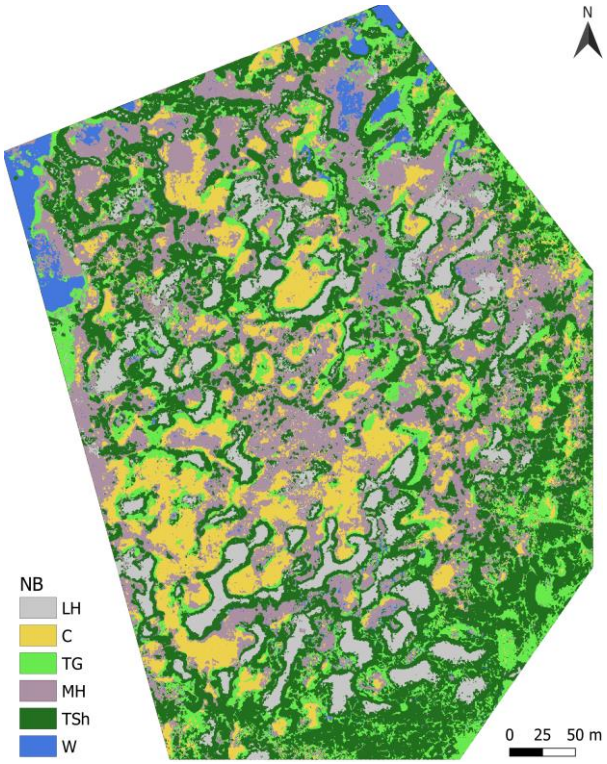

Figure 6. Land cover classification using the normal Bayes (NB) algorithm.

Table 4. Percentage distribution of land cover classes computed by three machine-learning algorithms.

Cover Type	Covered Area, %		
	NB	**RF**	**SVM**
lichen hummock vegetation (LH)	11	14	10
carpet vegetation (C)	13	13	14
tall graminoid vegetation (TG)	15	20	11
moist hummock vegetation (MH)	24	21	25
tall shrub vegetation (TSh)	33	30	37
open water(W)	3	3	3

Further, we used the model obtained by the NB method, since it is more accurate for most classes (Figure 6). We examined the mean values and standard deviations of morphometric parameters' distribution in LCC over all pixels for the NB model (Figure 7). For LCCs, an increase in variance for all parameters and insignificant deviations of the mean values were revealed in comparison with the training set. The most stable were the average values of absolute elevations; we found almost no differences. We observed the largest discrepancy across all LCCs for the slope, because it was of little value in the LCC prediction. According to the TPI data, for all classes, we observed a similar distribution as for the training sample. Simultaneously, the overall decrease in the TPI level for all pixels was through the training polygons' location closer to the large palsas. We identified for the TWI an increase in the dispersion of values, with LH and TSh classes being the most stable. These classes correlated to palsas and were characterized by less water accumulation and, equally, less variability of TWI values.

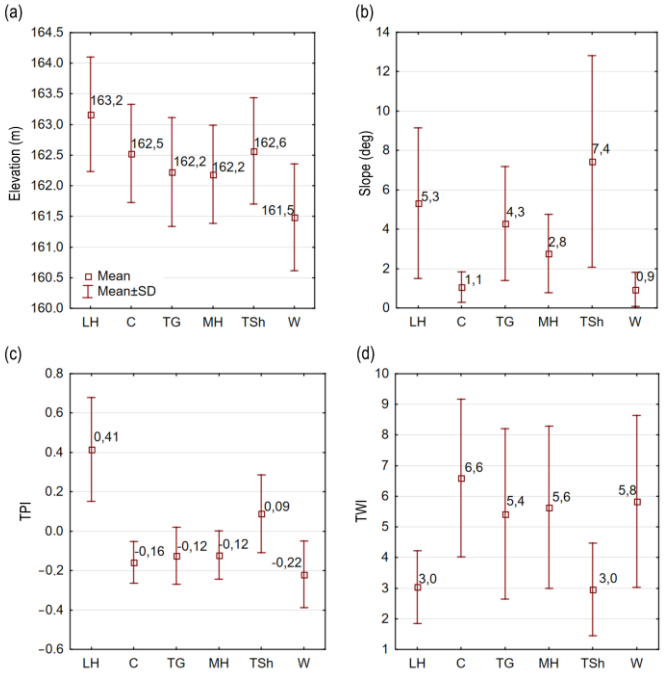

Figure 7. Means and standard deviations (SDs) of morphometric variable values for LCC over all image pixels (**a**)—elevation, (**b**)—slope, (**c**)—topographic position index, and (**d**)—topographic wetness index.

Finally, we identified the permafrost table in the GPR cross-sections, considering the LCC-based conclusion regarding the effect of permafrost condition on the classes' distribution. Having a single spatially referenced orthophoto, we could compare the peat deposit's interior structure against the distribution of the predictors and land cover classes on its surface. We identified three major GPR patterns in all the resultant cross-sections: (i) a clear interface at 0.3–0.8 m depth followed by abrupt signal attenuation, showing permafrost in palsas; (ii) a group of subparallel reflectors with sharp differences in amplitude, showing soaked peat, in particular because of permafrost thawing; (iii) wavy and discontinuous reflectors of varying intensity, bound on the bottom by an extensive interface, showing a regular peat layer and its boundary with the mineral bed. In fact, these patterns are quite typical of all palsa mires and GPR images of a similar kind have been described by Kohout et al. [65], Sjöberg et al. [47], and Jones et al. [79].

Figures 8 and 9 present the longitudinal and transversal GPR cross-sections of the study site with the respective TWI values and land cover classes according to the results of classification by the NB algorithm. After making a general comparison, we found a confident correlation between TWI < 3 with the LH class and the permafrost table position within the palsa, as well as for TWI > 5 with the C class and flarks with the most intensive horizontal reflectors. We deduced that palsas with permafrost were characterized by a certain sequence of classes reflected in GPR cross-sections. The top of the palsa was occupied by the LH class, which changed to TSh on the slope and then to C if there was meltwater accumulated upon permafrost thawing or, otherwise, to MH in drier habitats. This sequence of land cover classes appears in GPR cross-sections as a change from a pattern with a single extensive interface underlain by a signal attenuation zone at 60 ns to a pattern with high-amplitude subhorizontal reflectors showing at travel times exceeding 100 ns. Continuous GPR interfaces, uniform throughout their length, delineate areas where permafrost is still stable. Some palsas have narrow bands of TG vegetation along their edges, which may point to an activation of permafrost thawing. We defined this class in GPR cross-sections by local attenuation regions with a partial loss of the permafrost table interface. It is important to note that, if a palsa stands out in the relief but is permafrost-free, the said sequence of classes does not hold. The sequence LH–TSh–C, which we found to

indicate palsas with ongoing permafrost thawing, can be observed in profile 1, 220 m point (Figure 8a); profile 2, 15 m point (Figure 8b); profile 3, 35 m point (Figure 8c); profile 4, 155 m point (Figure 9a); and profile 5, 405 m point (Figure 9b). Sometimes, we noticed a non-symmetric layout of land cover classes regarding the palsa top. This may be evidence of variations in the rate and directivity of permafrost degradation across the area. The broken symmetry also shows in GPR cross-sections as changes in reflector intensity about the central axis of the palsa hummock (e.g., for palsas at 60, 90, and 200 m elevations in Section 1).

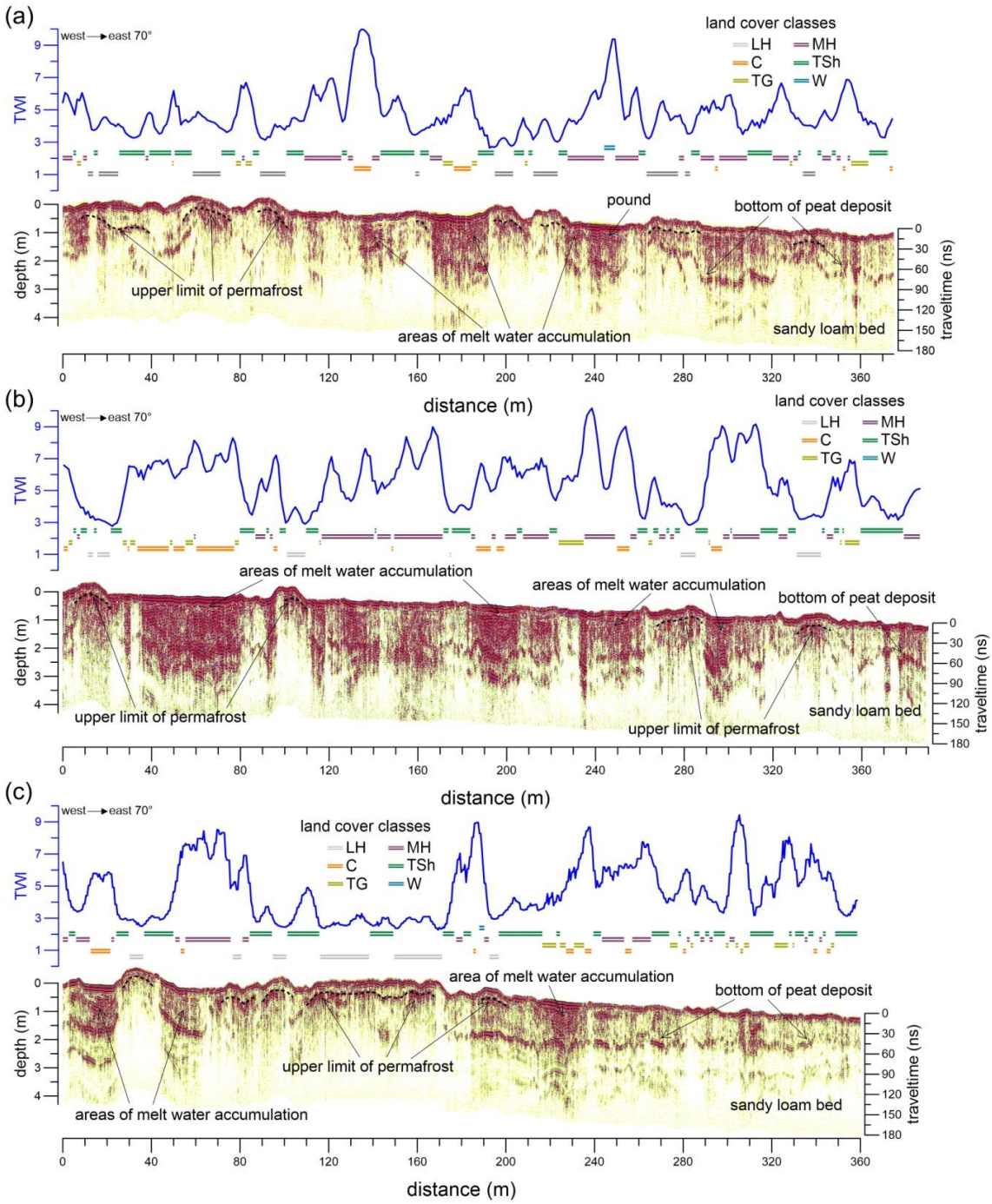

Figure 8. GPR cross-section, graph of TWI and LCC intervals from profiles GPR 1 (**a**), GPR 2 (**b**), and GPR 3 (**c**); dashed lines delineate permafrost table.

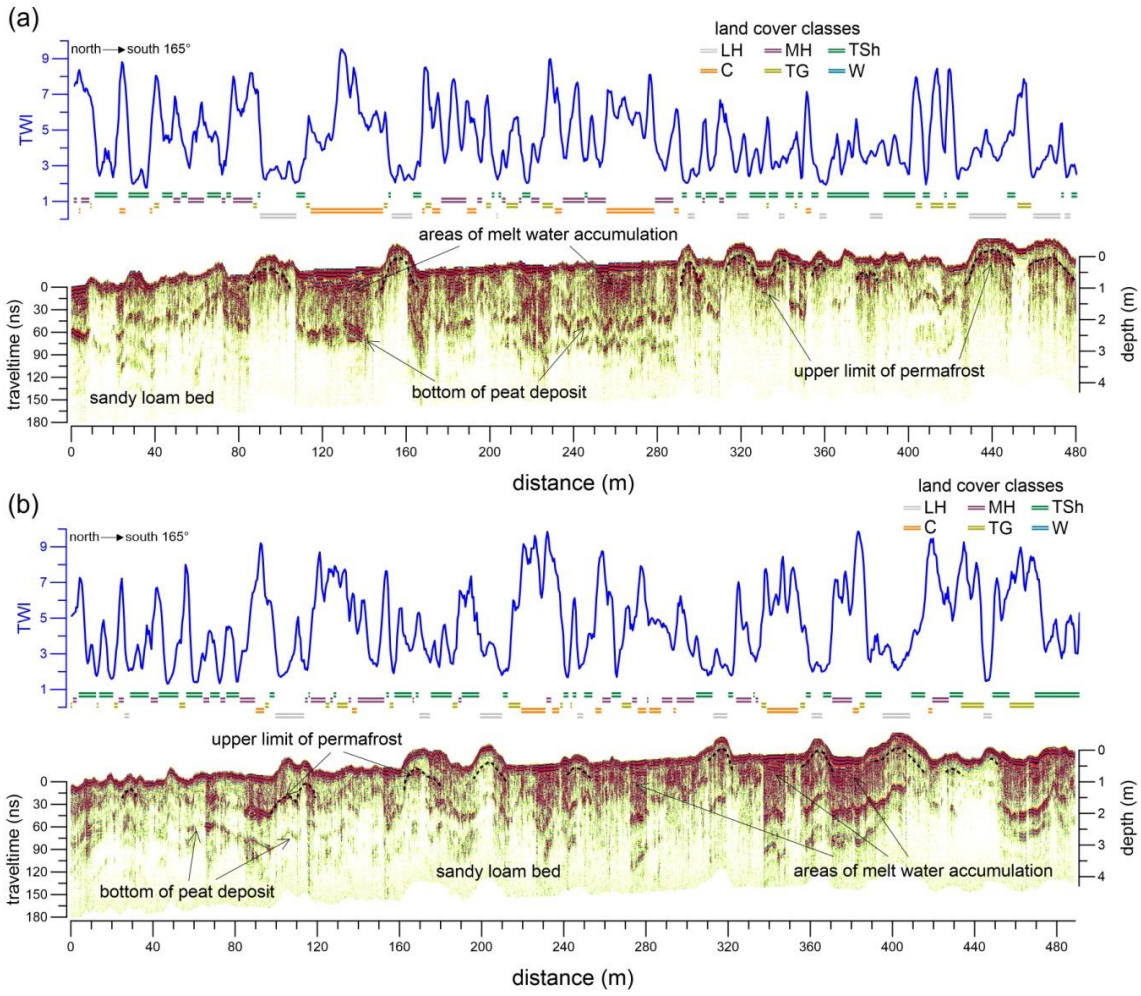

Figure 9. GPR cross-section, graph of TWI and LCC intervals from profiles GPR 4 (**a**) and GPR 5 (**b**); dashed lines delineate permafrost table.

Parts of investigated palsa mires with no frozen peat featured a mosaic arrangement of land cover classes. In individual cases, we depicted an abrupt change of classes after 2–3 m, which is a sign of a higher diversity of vegetation groups. Zuidhoff and Kolstrup [80] reported a rise in biodiversity as palsa degradation triggered the formation of new wet growing sites. The wave field of GPR cross-sections for such areas differed from what we observed in intervals with permafrost and is more typical of peatlands—extensive series of reflectors with local features of echo-signal amplitudes because of natural peat heterogeneity. We have confidently delineated an extended interface marking the top of the mineral base of the peat deposit. In addition, we defined reflectors generated by the underlying sand layers at GPR signal travel times greater than 120 ns. Such sequences of classes were the most explicit in profile 1 in the 350–375 m interval (Figure 8a), in profile 3 in the 220–360 m interval (Figure 8c), and in profile 6 in the 0–70 m interval (Figure 9b).

To show the relationship between the structure of the peat deposit and LCC in Figure 10, we have recognized marker GPR patterns. We observed that the C and MH classes have a greater intensity of GPR signal amplitudes related to peat humidity. When there was uniform peat moisture for the C class, we traced continuous reflectors on the GPR record. With unstable humidity for the MH class, the reflectors become more intermittent. LH–TSh classes on dry peat also have similar signal attenuation, which makes it easy to determine them. The identification internal specification of the TG class was more difficult, since, according to the TWI, it belongs to the wetness zones. However, GPR patterns did not confirm this. This land class formation was associated with the lateral melting

of permafrost in palsas. We assumed that the water coming from the palsa had a limited distribution in the thickness of the peat deposit. As a result, hygrophilous sphagnum moss grew up on the top soaked part (up to a depth of 70 cm), but below the peat remains dry. A further attenuation of the GPR signal could be associated with the remnants of permafrost at depth. Inclined or subvertical local zones with intense reflectors also characterized this class. We correlated them with erosion cracks in peat, which are filled with meltwater.

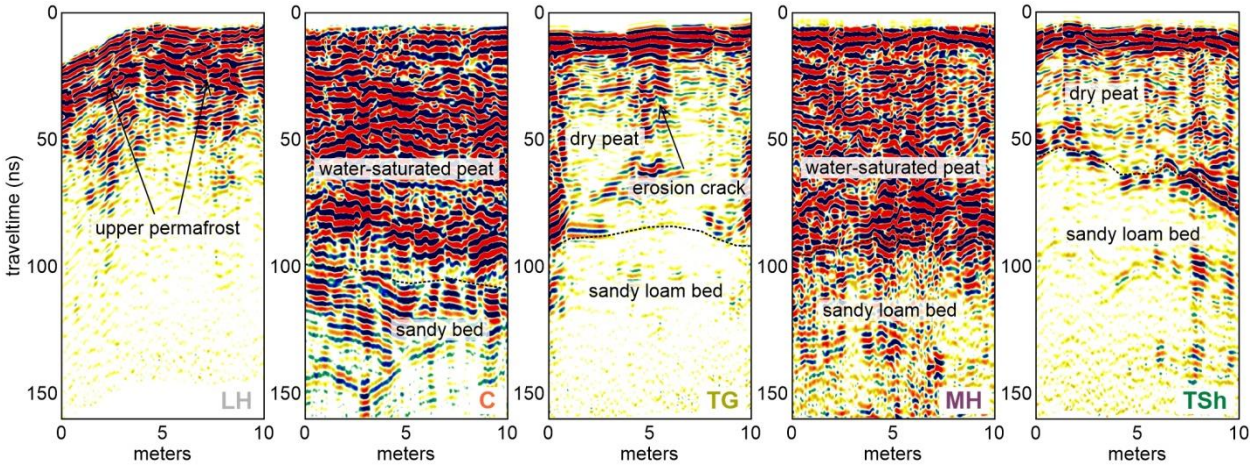

Figure 10. Fragments of GPR cross-sections illustrating GPR patterns under surfaces with different LCCs (NB algorithm).

8. Discussion

Predicting palsa dynamics requires an understanding of the set of processes associated with permafrost growth and degradation. We believe that the substantial time discreteness and time shift of the vegetation succession remote sensing data alone do not suffice for the accurate control of hummock collapse in palsa mires. Analysis of morphometric variables, such as palsa area, is not a reliable indicator of irreversible permafrost degradation, since palsas' growth and thaw can be altered by some seasonal anomalies. Therefore, simultaneous analysis of data on the interior structure of palsas, the shape and spatial distribution of permafrost, and the wetness of the peat deposit can help predict their climate resilience more accurately. The monitoring of palsa mires, which are often difficult to access, requires the application of combinations of remote sensing techniques. Thus, UAS-based surveying, which may be additionally combined with airborne GPR survey, may ultimately become the key method of palsa mire monitoring. Such technical solutions are now available [81], and subarctic and arctic territories can be a promising test ground, as they lack tall vegetation and can be surveyed by flying at low altitudes. GPR measurements made in a limited area of peatlands can provide ground reference points for processing data of large-scale remote sensing methods, such as inSAR. For example, variability in ecohydrology and peat density affects peat surface motion [82,83]. Therefore, the identification of these additional factors influencing the dynamism of the peatland ecosystem will simplify remote monitoring, preliminarily emphasizing areas of changes. With studying palsas, GPR data about the morphology and spatial distribution of permafrost can be used to predict areas of their collapse using SAR or LiDAR methods. In general, GPR is an actual component of digital soil mapping, including peatland [84].

Our findings confirm a correlation to exist between surface characteristics and the interior structure of palsa mires. For each identified LCC, we have found an original GPR pattern. Therefore, palsa monitoring is more efficient based on a sequence analysis of vegetation cover–surface morphology–peat internal structure, because all these elements have responses to external climatic impacts and are inseparable from each other. In this regard, prospects are opening for predicting the vegetation cover based on the surface

morphometry and internal features of peat. This can be useful where there are no ground observations or a low contrast of different vegetation classes in the optical range.

The GPR-determined thickness of the active layer on palsas in the surveyed site in July was 30–70 cm and 43 cm on average. These values fit in the 20–60 cm range of active layer measurements taken at this site in 1986 [50]. Thus, we have substantiated that active layer thickness is not so unequivocal as a predictor of permafrost condition and that both the exterior and the interior spatial structure of palsa mires should be monitored, and this agrees with current trends and discussions on this matter [85,86]. GPR data can be potentially used as additional predictors for machine learning, but the precondition is to decide on the required survey parameters and their expediency within the study design. The involvement of additional predictors can improve the quality of the classification of Subarctic peatlands. Namely, when considering a similar classification problem, Palace et al. [33] performed the analysis using RGB imagery supplemented with the results of textural analysis by artificial neural networks (ANNs). The final overall misclassification rate was 32%, and the authors remarked that SfM computing of topography can be added to machine learning to reduce the rate of pixel misclassification. Our results corroborate this statement, since the average overall error percentages for the algorithms were NB—12.8%, RF—23.2%, and SVM—17.7%. In research, we also encountered a problem of GPR and UAS data synchronization and consistency, which was mentioned by Yildiz et al. [66] previously. Thus, a unified algorithm has to be designed for merging predictors from different sources into a single GIS project.

At present, lateral degradation along the margins is regarded as the principal mechanism for areal loss of peat plateaus [79,85], which is valid also for palsa hummocks. The palsa area can be quantified from a DEM by the elevation of the inflection point of the plateau edge, whereas the exact location of the permafrost boundary is debatable [85]. Our GPR data underline that permafrost inside palsas may be irregular and does not always mirror the edge dynamics. We found a west-to-east asymmetry in the position of permafrost in some palsa hummocks (Figure 8a,b), whereas in the north-to-south direction (Figure 9a,b) the permafrost layer was usually symmetrical relative to the palsa shape. In the study area (Lovozero), winds in winter predominantly blow in the western direction, which may cause snow accumulation on the leeward side, on the eastern slope. This is another reason to consider the factor of snow cover thickness, corroborating the findings of Seppälä [15] and Martin et al. [85]. Thus, scenarios of permafrost degradation in palsa mires are to rely on accurate estimates of the current permafrost configuration in hummocks, their position relative to the surface morphology, and the probability of rapid collapse.

9. Conclusions

We performed integrated fieldwork and aerial surveying supplemented with GPR surveys for land cover clustering and analysis of vegetation and geomorphology patterns for a subarctic palsa mire in the central part of the Kola Peninsula. Our results verified the morphometric predictors' importance for machine learning since they improve the accuracy of LCC algorithms. However, we found that LCC may be equivocal in describing the permafrost condition in palsas. Our GPR data not only identified a high correlation with TWI values and LCC but also pinpointed some features of the vegetation cover shaped by the interior structure of the peat deposit and by the permafrost position. We assert that the condition of individual palsas can be revealed by identifying sequences of LCC classes, consistent with GPR patterns. Our results emphasize the need to expand the range of techniques for palsa mire diagnosis and monitoring, considering that the complex of UAS photogrammetry and GPR in our study delivered a more accurate delineation of lateral erosion areas of permafrost.

Supplementary Materials: The following supporting information can be downloaded at: https://www.mdpi.com/article/10.3390/rs15071896/s1, Figure S1. Aerial photography report; Figure S2. High-resolution orthophoto image in geoTIFF format; Figure S3. Images of land cover classification of the Lovozero palsa mire using normal Bayes, random forest, and support vector machines algorithms; Table S1: Error matrix (pixel count) for three algorithms.

Author Contributions: Conceptualization, P.R.; methodology, N.K. and P.R.; software, A.K.; validation, N.K. and P.I.; formal analysis, N.K.; investigation, P.R., P.I. and A.K.; resources, P.R., P.I. and A.K.; data curation, N.K. and P.I.; writing—original draft preparation, N.K. and P.R.; writing—review and editing, P.R., N.K. and P.I.; visualization, N.K. and A.K.; supervision, P.R.; project administration, P.R.; funding acquisition, P.R. All authors have read and agreed to the published version of the manuscript.

Funding: This research was funded by the Russian Science Foundation under grant No. 22-77-10055, https://rscf.ru/en/project/22-77-10055/ (accessed on 29 March 2023).

Data Availability Statement: All the UAS and GPR data are available on request from the corresponding author. The data are not publicly available due to the database size.

Conflicts of Interest: The authors declare no conflict of interest.

References

1. Hofgaard, A. Effects of climate change on the distribution and development of palsa peatlands: Background and suggestions for a national monitoring project. *NINA Proj. Rep.* **2003**, *21*, 1–32.
2. Luoto, M.; Heikkinen, R.K.; Carter, T.R. Loss of palsa mires in Europe and biological consequences. *Environ. Conserv.* **2004**, *31*, 30–37. [CrossRef]
3. Fronzek, S.; Carter, T.R.; Räisänen, J.; Ruokolainen, L.; Luoto, M. Applying probabilistic projections of climate change with impact models: A case study for sub-arctic palsa mires in Fennoscandia. *Clim. Change* **2010**, *99*, 515–534. [CrossRef]
4. Sannel, A.B.K.; Hugelius, G.; Jansson, P.; Kuhry, P. Permafrost Warming in a Subarctic Peatland—Which Meteorological Controls are Most Important? *Permafr. Periglac. Process.* **2016**, *27*, 177–188. [CrossRef]
5. Borge, A.F.; Westermann, S.; Solheim, I.; Etzelmüller, B. Strong degradation of palsas and peat plateaus in northern Norway during the last 60 years. *Cryosphere* **2017**, *11*, 1–16. [CrossRef]
6. Olvmo, M.; Holmer, B.; Thorsson, S.; Reese, H.; Lindberg, F. Sub-arctic palsa degradation and the role of climatic drivers in the largest coherent palsa mire complex in Sweden (Vissátvuopmi), 1955–2016. *Sci. Rep.* **2020**, *10*, 8937. [CrossRef]
7. Piilo, S.R.; Väliranta, M.M.; Amesbury, M.J.; Aquino-López, M.A.; Charman, D.J.; Gallego-Sala, A.; Garneau, M.; Koroleva, N.; Kärppä, M.; Laine, A.M.; et al. Consistent centennial-scale change in European sub-Arctic peatland vegetation toward Sphagnum dominance—Implications for carbon sink capacity. *Glob. Change Biol.* **2023**, *29*, 1530–1544. [CrossRef]
8. Fewster, R.E.; Morris, P.J.; Ivanovic, R.F.; Swindles, G.T.; Peregon, A.M.; Smith, C.J. Imminent loss of climate space for permafrost peatlands in Europe and Western Siberia. *Nat. Clim. Change* **2022**, *12*, 373–379. [CrossRef]
9. Könönen, O.H.; Karjalainen, O.; Aalto, J.; Luoto, M.; Hjort, J. Environmental spaces for palsas and peat plateaus are disappearing at a circumpolar scale. *Cryosphere Discuss.* **2022**. *preprint*. [CrossRef]
10. Sim, T.G.; Swindles, G.T.; Morris, P.J.; Baird, A.J.; Cooper, C.L.; Gallego-Sala, A.V.; Charman, D.J.; Roland, T.P.; Borken, W.; Mullan, D.J.; et al. Divergent responses of permafrost peatlands to recent climate change. *Environ. Res. Lett.* **2021**, *16*, 034001. [CrossRef]
11. Zhang, H.; Väliranta, M.; Swindles, G.T.; Aquino-López, M.A.; Mullan, D.; Tan, N.; Amesbury, M.; Babeshko, K.V.; Bao, K.; Bobrov, A.; et al. Recent Climate Change Has Driven Divergent Hydrological Shifts in High-Latitude Peatlands. *Nat. Commun.* **2022**, *13*, 4959. [CrossRef]
12. Biskaborn, B.K.; Smith, S.L.; Noetzli, J.; Matthes, H.; Vieira, G.; Streletskiy, D.A.; Schoeneich, P.; Romanovsky, V.E.; Lewkowicz, A.G.; Abramov, A.; et al. Permafrost is warming at a global scale. *Nat. Commun.* **2019**, *10*, 264. [CrossRef] [PubMed]
13. Seppälä, M. The origin of palsas. *Geogr. Ann. Ser. A* **1986**, *68*, 141–147. [CrossRef]
14. Gurney, S.D. Aspects of the genesis, geomorphology and terminology of palsas: Perennial cryogenic mounds. *Prog. Phys. Geogr.* **2001**, *25*, 249–260. [CrossRef]
15. Seppälä, M. Synthesis of studies of palsa formation underlining the importance of local environmental and physical characteristics. *Quat. Res.* **2011**, *75*, 366–370. [CrossRef]
16. Ballantyne, C.K. *Periglacial Geomorphology*; John Wiley & Sons: Hoboken, NJ, USA, 2018; 472 p.
17. Matthews, J.A.; Nesje, A. Scandinavia. In *Periglacial Landscapes of Europe*; Springer International Publishing: Cham, Switzerland, 2022; pp. 365–426. [CrossRef]
18. Jaworski, T. The morphology of peat bog surfaces on Hermansenøya, NW Svalbard. *Polar Sci.* **2017**, *11*, 83–95. [CrossRef]
19. Fillion, M.-È.; Bhiry, N.; Touazi, M. Differential Development of Two Palsa Fields in a Peatland Located near Whapmagoostui-Kuujjuarapik, Northern Québec, Canada. *Arct. Antarct. Alp. Res.* **2014**, *46*, 40–54. [CrossRef]
20. Jorgenson, M.T.; Harden, J.; Kanevskiy, M.; O'Donnell, J.; Wickland, K.; Ewing, S.; Manies, K.; Zhuang, Q.; Shur, Y.; Striegl, R.; et al. Reorganization of vegetation, hydrology and soil carbon after permafrost degradation across heterogeneous boreal landscapes. *Environ. Res. Lett.* **2013**, *8*, 035017. [CrossRef]
21. Mamet, S.D.; Chun, K.P.; Kershaw, G.G.; Loranty, M.M.; Kershaw, P.G. Recent increases in permafrost thaw rates and areal loss of palsas in the Western Northwest Territories, Canada. *Permafr. Periglac. Process.* **2017**, *28*, 619–633. [CrossRef]
22. Jean, M.; Payette, S. Effect of vegetation cover on the ground thermal regime of wooded and non-wooded palsas. *Permafr. Periglac. Process.* **2014**, *25*, 281–294. [CrossRef]

23. Limpens, J.; Fijen, T.P.; Keizer, I.; Meijer, J.; Olsthoorn, F.; Pereira, A.; Postma, R.; Suyker, M.; Vasander, H.; Holmgren, M. Shrubs and degraded permafrost pave the way for tree establishment in subarctic peatlands. *Ecosystems* **2021**, *24*, 370–383. [CrossRef]
24. Turetsky, M.R.; Bond-Lamberty, B.; Euskirchen, E.; Talbot, J.; Frolking, S.; McGuire, A.D.; Tuittila, E.S. The resilience and functional role of moss in boreal and arctic ecosystems. *New Phytol.* **2012**, *196*, 49–67. [CrossRef] [PubMed]
25. Zhang, H.; Piilo, S.R.; Amesbury, M.J.; Charman, D.J.; Gallego-Sala, A.V.; Väliranta, M.M. The role of climate change in regulating Arctic permafrost peatland hydrological and vegetation change over the last millennium. *Quat. Sci. Rev.* **2018**, *182*, 121–130. [CrossRef]
26. Brown, J.; Ferrians, O.; Heginbottom, J.A.; Melnikov, E. *Circum-Arctic Map of Permafrost and Ground-Ice Conditions*; Version 2; National Snow and Ice Data Center: Boulder, CO, USA, 2002. [CrossRef]
27. Romanenko, F.A.; Garankina, E.V. Permafrost formation and structure at the south border of cryolithozone, the Kola Peninsula. *Earth's Cryosphere* **2012**, *16*, 72–80.
28. Gisnås, K.; Etzelmüller, B.; Lussana, C.; Hjort, J.; Sannel, A.B.K.; Isaksen, K.; Westermann, S.; Kuhry, P.; Christiansen, H.H.; Frampton, A.; et al. Permafrost map for Norway, Sweden and Finland. *Permafr. Periglac. Process.* **2016**, *28*, 359–378. [CrossRef]
29. Barcan, V.S. Stability of palsa at the southern margin of its distribution on the Kola Peninsula. *Polar Sci.* **2010**, *4*, 489–495. [CrossRef]
30. Marshall, G.J.; Vignols, R.M.; Rees, W.G. Climate Change in the Kola Peninsula, Arctic Russia, during the Last 50 Years from Meteorological Observations. *J. Clim.* **2016**, *29*, 6823–6840. [CrossRef]
31. Koptseva, E.M.; Natsvaladze, N.Y.; Zhuravleva, E.N. Transformation of palsa mires vegetation on Kola Peninsula under climatic changes. *Bot. Zhurnal* **2016**, *101*, 537–547.
32. Kutenkov, S.A.; Kozhin, M.N.; Golovina, E.O.; Kopeina, E.I.; Stoikina, N.V. Polygonal patterned peatlands of the White Sea islands. *IOP Conf. Ser. Earth Environ. Sci.* **2018**, *138*, 012010. [CrossRef]
33. Palace, M.; Herrick, C.; DelGreco, J.; Finnell, D.; Garnello, A.J.; McCalley, C.; McArthur, K.; Sullivan, F.; Varner, R.K. Determining Subarctic Peatland Vegetation Using an Unmanned Aerial System (UAS). *Remote Sens.* **2018**, *10*, 1498. [CrossRef]
34. de la Barreda-Bautista, B.; Boyd, D.S.; Ledger, M.; Siewert, M.B.; Chandler, C.; Bradley, A.V.; Gee, D.; Large, D.J.; Olofsson, J.; Sowter, A.; et al. Towards a Monitoring Approach for Understanding Permafrost Degradation and Linked Subsidence in Arctic Peatlands. *Remote Sens.* **2022**, *14*, 444. [CrossRef]
35. He, C.; Zhang, J.; Liu, Z.; Huang, Q. Characteristics and Progress of Land Use/Cover Change Research during 1990–2018. *J. Geogr. Sci.* **2022**, *32*, 537–559. [CrossRef]
36. Räsänen, A.; Aurela, M.; Juutinen, S.; Kumpula, T.; Lohila, A.; Penttilä, T.; Virtanen, T. Detecting northern peatland vegetation patterns at ultra-high spatial resolution. *Remote Sens. Ecol. Conserv.* **2020**, *6*, 457–471. [CrossRef]
37. Räsänen, A.; Virtanen, T. Data and resolution requirements in mapping vegetation in spatially heterogeneous landscapes. *Remote Sens. Environ.* **2019**, *230*, 111207. [CrossRef]
38. Siewert, M.B.; Olofsson, J. Scale-dependency of Arctic ecosystem properties revealed by UAV. *Environ. Res. Lett.* **2020**, *15*, 094030. [CrossRef]
39. Thomson, E.R.; Spiegel, M.P.; Althuizen, I.H.J.; Bass, P.; Chen, S.; Chmurzynski, A.; Halbritter, A.H.; Henn, J.J.; Jónsdóttir, I.S.; Klanderud, K.; et al. Multiscale Mapping of Plant Functional Groups and Plant Traits in the High Arctic Using Field Spectroscopy, UAV Imagery and Sentinel-2A Data. *Environ. Res. Lett.* **2021**, *16*, 055006. [CrossRef]
40. Cunnick, H.; Ramage, J.M.; Magness, D.; Peters, S.C. Mapping Fractional Vegetation Coverage across Wetland Classes of Sub-Arctic Peatlands Using Combined Partial Least Squares Regression and Multiple Endmember Spectral Unmixing. *Remote Sens.* **2023**, *15*, 1440. [CrossRef]
41. Hugelius, G.; Virtanen, T.; Kaverin, D.; Pastukhov, A.; Rivkin, F.; Marchenko, S.; Romanovsky, V.; Kuhry, P. High-resolution mapping of ecosystem carbon storage and potential effects of permafrost thaw in periglacial terrain, European Russian Arctic. *J. Geophys. Res. Biogeosci.* **2011**, *116*, G03024. [CrossRef]
42. Siewert, M.B.; Hanisch, J.; Weiss, N.; Kuhry, P.; Maximov, T.C.; Hugelius, G. Comparing carbon storage of Siberian tundra and taiga permafrost ecosystems at very high spatial resolution: Ecosystem carbon in taiga and tundra. *J. Geophys. Res. Biogeosci.* **2015**, *120*, 1973–1994. [CrossRef]
43. Siewert, M.B. High-resolution digital mapping of soil organic carbon in permafrost terrain using machine learning: A case study in a sub-Arctic peatland environment. *Biogeosciences* **2018**, *15*, 1663–1682. [CrossRef]
44. Sjogersten, S.; Ledger, M.; Siewert, M.; de la Barreda-Bautista, B.; Sowter, A.; Gee, D.; Foody, G.; Boyd, D.S. Capabilities of optical and radar Earth observation data for up-scaling methane emissions linked to subsidence and permafrost degradation in sub-Arctic peatlands. *Biogeosci. Discuss.* **2023**. *preprint*. [CrossRef]
45. Douglas, T.A.; Jorgenson, M.T.; Brown, D.R.; Campbell, S.W.; Hiemstra, C.A.; Saari, S.P.; Bjella, K.; Liljedahl, A.K. Degrading permafrost mapped with electrical resistivity tomography, airborne imagery and LiDAR, and seasonal thaw measurements. *Geophysics* **2016**, *81*, WA71–WA85. [CrossRef]
46. Douglas, T.A.; Hiemstra, C.A.; Anderson, J.E.; Barbato, R.A.; Bjella, K.L.; Deeb, E.J.; Gelvin, A.B.; Nelsen, P.E.; Newman, S.D.; Saari, S.P.; et al. Recent degradation of Interior Alaska permafrost mapped with ground surveys, geophysics, deep drilling, and repeat airborne LiDAR. *Cryosphere* **2021**, *15*, 3555–3575. [CrossRef]
47. Sjöberg, Y.; Marklund, P.; Pettersson, R.; Lyon, S.W. Geophysical mapping of palsa peatland permafrost. *Cryosphere* **2015**, *9*, 465–478. [CrossRef]

48. Emmert, A.; Kneisel, C. Internal structure and palsa development at Orravatnsrústir Palsa Site (Central Iceland), investigated by means of integrated resistivity and ground-penetrating radar methods. *Permafr. Periglac. Process.* **2021**, *32*, 503–519. [CrossRef]
49. Martin, L.C.P.; Nitzbon, J.; Aas, K.S.; Etzelmüller, B.; Kristiansen, H.; Westermann, S. Stability conditions of peat plateaus and palsas in northern Norway. *J. Geophys. Res. Earth Surf.* **2019**, *124*, 705–719. [CrossRef]
50. Elina, G.A.; Lukashov, A.D.; Yurkovskaya, T.K. *Late Glacial and Holocene Palaeovegetation and Palaeogeography of Eastern Fennoscandia*; The Finnish Environmental Institute: Helsinki, Finland, 2010; ISBN 978-952-11-3715-0.
51. Batuev, V.I.; Kalyuzhny, I.L. Hydrological regime and freezing of hummocky bogs on the European North of Russia. *Eng. Surv.* **2018**, *12*, 38–48. [CrossRef]
52. Danielson, J.J.; Gesch, D.B. Global Multi-resolution Terrain Elevation Data 2010 (GMTED2010). Open-File Report 2011–1073. U.S. Department of the Interior; U.S. Geological Survey. Available online: https://pubs.usgs.gov/of/2011/1073/pdf/of2011-1073.pdf (accessed on 25 January 2023).
53. Ecke, S.; Dempewolf, J.; Frey, J.; Schwaller, A.; Endres, E.; Klemmt, H.-J.; Tiede, D.; Seifert, T. UAV-Based Forest Health Monitoring: A Systematic Review. *Remote Sens.* **2022**, *14*, 3205. [CrossRef]
54. Müllerová, J.; Gago, X.; Bučas, M.; Company, J.; Estrany, J.; Fortesa, J.; Manfreda, S.; Michez, A.; Mokroš, M.; Paulus, G.; et al. Characterizing Vegetation Complexity with Unmanned Aerial Systems (UASs)—A Framework and Synthesis. *Ecological Indicators* **2021**, *131*, 108156. [CrossRef]
55. Wolff, F.; Kolari, T.H.; Villoslada, M.; Tahvanainen, T.; Korpelainen, P.; Zamboni, P.A.; Kumpula, T. RGB vs. Multispectral imagery: Mapping aapa mire plant communities with UAVs. *Ecol. Indic.* **2023**, *148*, 110140. [CrossRef]
56. Steenvoorden, J.; Bartholomeus, H.; Limpens, J. Less is more: Optimizing vegetation mapping in peatlands using unmanned aerial vehicles (UAVs). *Int. J. Appl. Earth Obs. Geoinf.* **2023**, *117*, 103220. [CrossRef]
57. Verdonen, M.; Tarolli, P.; Korpelainen, P.; Kolari, T.; Tahvanainen, T.; Kumpula, T. Application of UAS in the analysis of the spatial distribution of active layer thickness in Palsa mounds. *Geophys. Res. Abstr.* **2019**, *21*, 13158.
58. Westoby, M.J.; Brasington, J.; Glasser, N.F.; Hambrey, M.J.; Reynolds, J. Structure-from-Motion photogrammetry: A low-cost, effective tool for geoscience applications. *Geomorphology* **2012**, *179*, 300–314. [CrossRef]
59. Annan, A.P. Electromagnetic Principles of Ground Penetrating Radar. In *Ground Penetrating Radar: Theory and Applications*; Jol, H.M., Ed.; Elsevier: Amsterdam, The Netherlands, 2009; pp. 1–40. ISBN 978-044-453-348-7.
60. Arcone, S.A.; Lawson, D.E.; Delaney, A.J.; Strasser, J.C.; Strasser, J.D. Ground-penetrating radar reflection profiling of groundwater and bedrock in an area of discontinuous permafrost. *Geophysics* **1998**, *63*, 1573–1584. [CrossRef]
61. Moorman, B.J.; Robinson, S.D.; Burgess, M.M. Imaging periglacial conditions with ground-penetrating radar. *Permafr. Periglac. Process.* **2003**, *14*, 319–329. [CrossRef]
62. Kneisel, C.; Hauck, C.; Fortier, R.; Moorman, B. Advances in Geophysical Methods for Permafrost Investigations. *Permafr. Periglac. Process.* **2008**, *19*, 157–178. [CrossRef]
63. Doolittle, J.A.; Hardisky, M.A.; Black, S. A ground-penetrating radar study of Goodream palsas, Newfoundland, Canada. *Arct. Alp. Res.* **1992**, *24*, 173–178. [CrossRef]
64. Horvath, C.L. An evaluation of ground penetrating radar for investigation of palsa evolution, Macmillan Pass, NWT, Canada. In *Permafrost: Seventh International Conference Proceedings, Yellowknife, NT, Canada, 23–27 June 1998*; Lewkowicz, A.G., Allard, M., Eds.; Centre d'études Nordiques, Universite Laval: Québec, QC, Canada; pp. 473–478.
65. Kohout, T.; Bućko, M.S.; Rasmus, K.; Leppäranta, M.; Matero, I. Non-Invasive Geophysical Investigation and Thermodynamic Analysis of a Palsa in Lapland, Northwest Finland. *Permafr. Periglac. Process.* **2014**, *25*, 45–52. [CrossRef]
66. Yildiz, S.; Akyurek, Z.; Binley, A. Quantifying snow water equivalent using terrestrial ground penetrating radar and unmanned aerial vehicle photogrammetry. *Hydrol. Process.* **2021**, *35*, e14190. [CrossRef]
67. Pal, M. Random Forest classifier for remote sensing classification. *Int. J. Remote Sens.* **2005**, *26*, 217–222. [CrossRef]
68. Pal, M.; Mather, P.M. Support vector machines for classification in remote sensing. *Int. J. Remote Sens.* **2005**, *26*, 1007–1011. [CrossRef]
69. Kotsiantis, S.B. Supervised Machine Learning: A Review of Classification Techniques. *Informatica* **2007**, *31*, 249–268.
70. Cracknell, M.J.; Reading, A.M. Geological mapping using remote sensing data: A comparison of five machine learning algorithms, their response to variations in the spatial distribution of training data and the use of explicit spatial information. *Comput. Geosci.* **2014**, *63*, 22–33. [CrossRef]
71. Chen, S.; Webb, G.I.; Liu, L.; Ma, X. A novel selective naïve Bayes algorithm. *Knowl.-Based Syst.* **2020**, *192*, 105361. [CrossRef]
72. Nayak, J.; Naik, B.; Behera, H.S. A Comprehensive Survey on Support Vector Machine in Data Mining Tasks: Applications & Challenges. *Int. J. Database Theory Appl.* **2015**, *8*, 169–186. [CrossRef]
73. Breiman, L. Random Forests. *Mach. Learn.* **2001**, *45*, 5–32. [CrossRef]
74. Wilson, M.F.J.; O'Connell, B.; Brown, C.; Guinan, J.C.; Grehan, A.J. Multiscale Terrain Analysis of Multibeam Bathymetry Data for Habitat Mapping on the Continental Slope. *Mar. Geod.* **2007**, *30*, 3–35. [CrossRef]
75. Moore, I.D.; Grayson, R.B.; Ladson, A.R. Digital terrain modelling: A review of hydrological, geomorphological, and biological applications. *Hydrol. Process.* **1991**, *5*, 3–30. [CrossRef]
76. Weiss, A.D. Topographic Position and Landforms Analysis. In Proceedings of the Poster Presentation, ESRI User Conference, San Diego, CA, USA, 9–13 July 2001.

77. Congalton, R.G. A review of assessing the accuracy of classifications of remotely sensed data. *Remote Sens. Environ.* **1991**, *37*, 35–46. [CrossRef]
78. Conrad, O.; Bechtel, B.; Bock, M.; Dietrich, H.; Fischer, E.; Gerlitz, L.; Wehberg, J.; Wichmann, V.; Böhner, J. System for automated geoscientific analyses (SAGA) v. 2.1.4. *Geosci. Model Dev.* **2015**, *8*, 1991–2007. [CrossRef]
79. Jones, B.M.; Baughman, C.A.; Romanovsky, V.E.; Parsekian, A.D.; Babcock, E.L.; Stephani, E.; Jones, M.C.; Grosse, G.; Berg, E.E. Presence of rapidly degrading permafrost plateaus in south-central Alaska. *Cryosphere* **2016**, *10*, 2673–2692. [CrossRef]
80. Zuidhoff, F.S.; Kolstrup, E. Palsa development and associated vegetation in northern Sweden. *Arct. Antarct. Alp. Res.* **2005**, *37*, 49–60. [CrossRef]
81. Noviello, C.; Gennarelli, G.; Esposito, G.; Ludeno, G.; Fasano, G.; Capozzoli, L.; Soldovieri, F.; Catapano, I. An Overview on Down-Looking UAV-Based GPR Systems. *Remote Sens.* **2022**, *14*, 3245. [CrossRef]
82. Marshall, C.; Sterk, H.P.; Gilbert, P.J.; Andersen, R.; Bradley, A.V.; Sowter, A.; Marsh, S.; Large, D.J. Multiscale Variability and the Comparison of Ground and Satellite Radar Based Measures of Peatland Surface Motion for Peatland Monitoring. *Remote Sens.* **2022**, *14*, 336. [CrossRef]
83. Bradley, A.V.; Andersen, R.; Marshall, C.; Sowter, A.; Large, D.J. Identification of typical ecohydrological behaviours using InSAR allows landscape-scale mapping of peatland condition. *Earth Surf. Dyn.* **2022**, *10*, 261–277. [CrossRef]
84. Minasny, B.; Berglund, Ö.; Connolly, J.; Hedley, C.; de Vries, F.; Gimona, A.; Kempen, B.; Kidd, D.; Lilja, H.; Malone, B.; et al. Digital Mapping of Peatlands—A Critical Review. *Earth-Sci. Rev.* **2019**, *196*, 102870. [CrossRef]
85. Martin, L.C.P.; Nitzbon, J.; Scheer, J.; Aas, K.S.; Eiken, T.; Langer, M.; Filhol, S.; Etzelmüller, B.; Westermann, S. Lateral thermokarst patterns in permafrost peat plateaus in northern Norway. *Cryosphere* **2021**, *15*, 3423–3442. [CrossRef]
86. Verdonen, M.; Störmer, A.; Korpelainen, P.; Lotsari, E.; Burkhard, B.; Colpaert, A.; Kumpula, T. Permafrost degradation at two monitored palsa mires in north-west Finland. *EGUsphere* **2022**. *preprint*. [CrossRef]